Insights into the thermopower of thermally regenerative electrochemical cycle for low grade heat harvesting

Chun Cheng[1], Sijia Wang[2], Peng Tan[3], Yawen Dai[1], Jie Yu[1], Rui Cheng[2], Shien-Ping Feng[2], Meng Ni[1]**

1 Department of Building and Real Estate, The Hong Kong Polytechnic University, Hung Hom, Kowloon, Hong Kong, China

2 Department of Mechanical Engineering, The University of Hong Kong, Pokfulam Road, Hong Kong, China

3 Department of Thermal Science and Energy Engineering, University of Science and Technology of China (USTC), Hefei, Anhui, China

ABSTRACT

Thermally regenerative electrochemical cycle (TREC) is a promising technology for converting low-grade heat (<100 ºC) to electrical power. In this work, the TREC with NiHCF cathode and Zn anode achieves a markedly high thermopower (α) of -1.575 mV K^{-1} and a heat-to-electricity efficiency of 2.41% at the temperature difference of 30 ℃ (equivalent to 25.15% of Carnot

efficiency), surpassing all the existing TREC systems. For the first time, the mixed membranes with mixed pH electrolytes is introduced in the TREC systems to boost *α to* a record-high value of -2.270 mV K^{-1}. The proposed thermodynamic framework advances the understanding on the origin of *α* and electrochemical potential, which will guide people to engineer TRECs.

TOC GRAPHICS

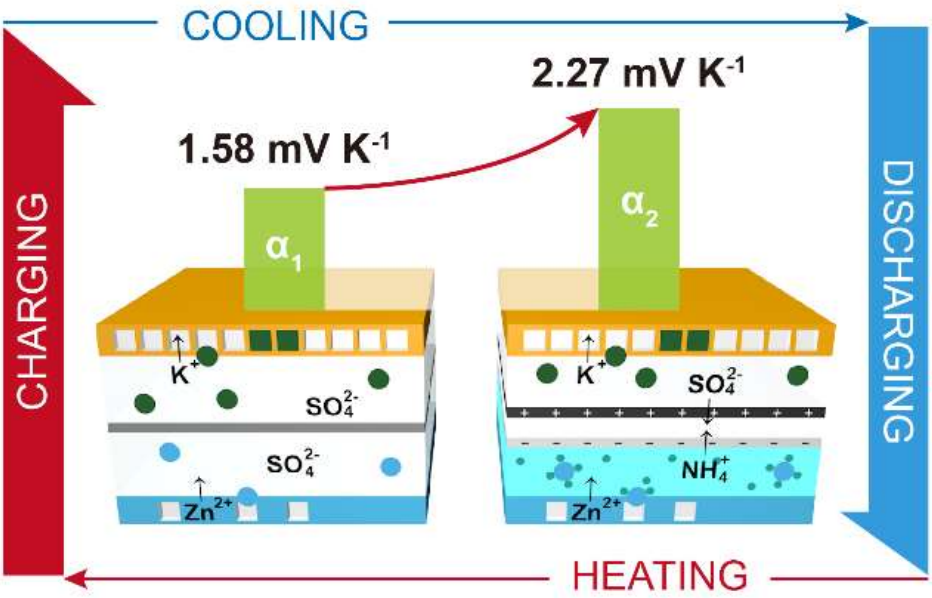

MAIN TEXT

Low-grade heat is abundantly available in the form of waste heat or in the environment.[1] Converting the low-grade heat to electrical power will significantly help the energy saving and carbon emission reduction, yet its efficient recovery is still a great challenge. One key reason is the low α ($\alpha = \frac{\Delta E}{\Delta T}$: V K^{-1}) in the existing thermoelectric devices. Considering a redox couple whose two electrodes operate at different temperatures, the electromotive force can be written as $\Delta E^0 = E^0(T + \Delta T) - E^0(T) = \alpha \Delta T$, where E^0 is the standard electrode potential of the redox pair, and α is defined as the ratio of potential difference to the temperature change, indicating the ability to produce voltage per unit temperature difference. It is also known as Seebeck coefficient in the solid-state thermoelectric generators (TEs) field. However, the conventional TEs utilize narrow-gap semiconductors with the α in the scale of 100 - 200 μV K^{-1}, limiting the voltage generation and power output when operating in a small temperature difference at low-grade heat regime. Therefore a number of liquid-based technologies are emerging nowadays,[2] such as thermo-osmotic energy conversion (TOEC) systems which exploit thermo-osmotic vapour transport through membranes,[3] thermally regenerative batteries (TRBs) which utilize ammonia adsorption to establish a voltage difference,[4] thermoelectrochemical cells (TECs) which take advantage of temperature response redox couple to produce electricity from heat source.[5] Particularly TECs could potentially provide cost-effective and scalable approach for low-grade heat harvesting, as their temperature coefficient (mV K^{-1}) is one order of magnitude higher than that of TE semiconductors. For example, the TECs using typical $[Fe(CN)_6]^{3-}/[Fe(CN)_6]^{4-}$ redox couple presents an α of -1.42 mV K^{-1}.[6] And the value could be optimized to -3.73 mV K^{-1} by thermosensitive crystallization and dissolution process.[5] However, the large distance is needed between two electrodes to maintain the temperature difference and sustain the desired redox

reactions in each side of the electrode, of which poor ionic conductivity and huge Ohmic loss cause small current output and thus low efficiency. Alternatively, TREC exploits thermal cycle so that the distance between hot and cold electrodes can be shortened to improve the ionic conductance and reach a high efficiency.[7]

In TREC systems, the α is calculated by $\alpha = \frac{\Delta E}{\Delta T} = \frac{\Delta S}{nF}$, where n is the number of transferred electrons in the electrochemical reaction, F is Faraday's constant, and ΔS is entropy change of the electrochemical reaction.[8] As the α determines the theoretical voltage at the specific operating temperatures, it is critical to the achievable power output and energy efficiency. Efforts have been made to enlarge the α by increasing the reaction entropy change (ΔS).[9] As the fundamental understanding of the origin of α is critical for further improving the TREC system, a series of Prussian blue analogs (PBA) such as copper hexacyanoferrate (CuHCF),[10] nickel hexacyanoferrate (NiHCF),[8] cobalt hexacyanoferrate (CoHCF)[11] have been studied to explore the entropy change of their intercalation reaction to enlarge the thermopower. It is found the thermopower of PBA is corresponding to the lattice status, and the entropy change ΔS could be divided into ion entropy, phonon vibration entropy, configuration entropy, electron entropy and other entropy.[11] In addition to PBA, metal complex redox systems including TRBs have been widely explored. They mainly rely on the ligand adsorption such as ammonia to create a voltage gap from two reactions. In other words, the thermal induced phase change produces a energy gap to harvest waste heat. [12, 13, 14, 15, 16, 17, 18]

In this work, a modified Nernst equation was derived to determine the theoretical voltage and temperature-dependent reaction energy. Moreover, the fundamental thermodynamics and kinetics process of potassium ion (K^+) intercalation to nickel hexacyanoferrate (NiHCF) electrode was established to build a theoretical framework. The TREC with NiHCF cathode and Zn anode

achieved a markedly high α of -1.575 mV K^{-1} and a heat-to-electricity efficiency (η) of 2.41% at the temperature difference of 30 ℃ (equivalent to 25.15% of Carnot efficiency, η_C). By introducing mixed membranes, the α was boosted up to a record high value of -2.270 mV K^{-1} compared to all the existing TREC systems. It is noted that the TREC efficiency can be readily increased by heat recuperation because part of the heat rejected in cooling step can be used for heating step.

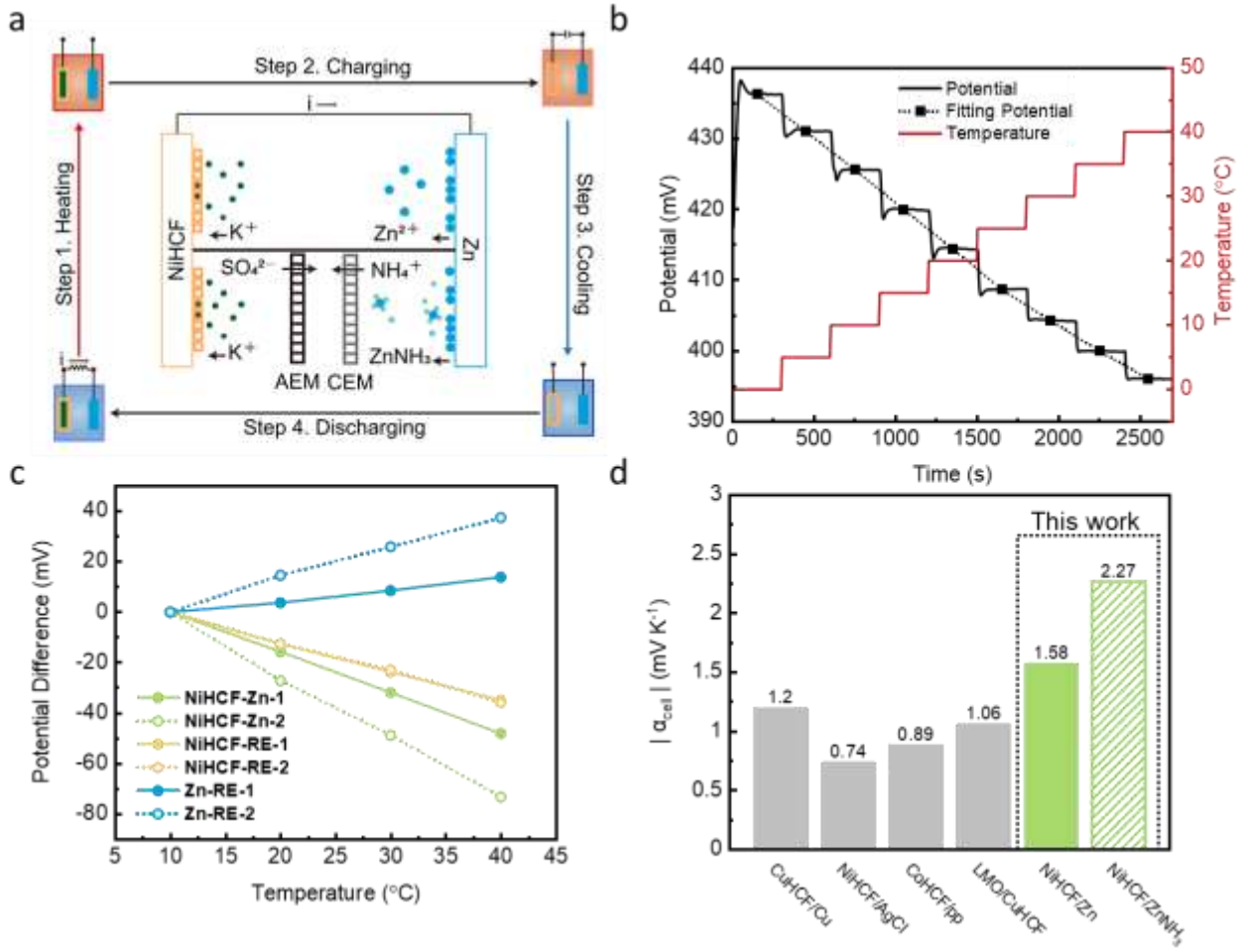

Figure 1. Working diagram of TREC and α performance of cathode, anode and the cell. **a)** The four steps working principle of TREC and the discharging reaction of NiHCF/Zn and NiHCF/$ZnNH_3$ system. **b)** The cathode voltage response to the temperature from 0°C to 40°C. **c)** The NiHCF, Zn vs. RE (AgCl/Ag) and full cell voltage difference change with temperature

difference of 30℃. 1 represents NiHCF/K_2SO_4/Zn system, 2 represents NiHCF/ K_2SO_4//NH_3+$(NH_4)_2SO_4$ +$ZnSO_4$/Zn system. **d)** The comparison on absolute α value of different systems including CuHCF/Cu,[10] NiHCF/AgCl,[8] CoHCF/pp[9] and LMO/CuHCF,[19] green marked bars are our work.

As is shown in Figure 1a, the energy conversion process includes four steps: heating up, charging, cooling down and finally discharging. When the system is heated to a high temperature (T_H), the open circuit voltage (OCV) decreases ($V(T_H)$) in the first step. Then system is charged in the second step. When the system is cooled down to a low temperature (T_L), the OCV increases ($V(T_L)$) to a voltage higher than $V(T_H)$. Finally, the discharging process is conducted at a low temperature. In such a cycle, the low grade heat energy is utilized to create potential difference so that the system can be charged at a lower voltage ($V(T_H)$) and discharged at a higher voltage ($V(T_L)$), producing net electrical energy. The change in electric potential per unit temperature difference is defined as α in equation 1, which is also called temperature coefficient for liquid-based system, or Seebeck coefficient for thermoelectric materials.

$$\alpha = \frac{V(T_H)-V(T_L)}{T_H-T_L} = \frac{\Delta S}{nF} \quad (1)$$

n is the number of transferred electrons per reaction. F is the Faraday Constant. S is the entropy. Both the efficiency and power output of the system are highly dependent on α. In order to obtain a higher efficiency and power output, a larger α is required to provide a larger potential difference. Here, we applied NiHCF as cathode and Zn as anode. The two half reactions are given as formula 2 and 3:

$$KNi^{II}Fe^{III}(CN)_6 + K^+ + e^- \rightarrow K_2Ni^{II}Fe^{II}(CN)_6 \quad (2)$$

$$Zn \rightarrow Zn^{2+} + 2e^- \quad (3)$$

In this system, potassium ions intercalate into the electrode materials while Zn dissolves into the electrolyte during discharging process. NiHCF nanoparticles were synthesized by dropping both 10 mM $NiCl_2$ aqueous solution and 5 mM $KNiFe(CN)_6$ aqueous solution into 50℃ deionized water with stirring. The average particle size is about 200 nm (Supplementary Figure 1). The anode was prepared by ultrasonic cleaning the pure zinc plate. The electrolyte was 0.5 M K_2SO_4 aqueous solution. Because of the active properties of zinc, the neutral pH (~6.5) solution helped to minimize the zinc corrosion. Zinc was stabilized by K_2SO_4 electrolyte. The cathode, anode and separator were assembled in a pouch cell.

As is shown in Figure 1b, the OCV changes quickly with the temperature while the α is the slope of the fitting potential. From the fitting slope of Figure 1b, the optimized NiHCF achieves an average α of -0.875 mV K^{-1} (-0.720 mV K^{-1} ~ -1.176 mV K^{-1}), while Zn presents an average α of +0.700 mV K^{-1} (+0.608 mV K^{-1} ~ +0.79 mV K^{-1}). Thus, the overall α of the full cell reaches -1.575 mV K^{-1} (-1.403 mV K^{-1} ~ -1.752 mV K^{-1}).

Previous researches focused on the cathode development to increase the α due to the difficulty in adjusting the entropy change of anode reaction in single neutral electrolyte. Because of the low α of metal, adjusting reaction entropy of the zinc electrode instead of improving the material properties could be an effective way to enhance the α. Thus, a coordination reaction can be used because it brings extra reactant to change the reaction entropy change. To enlarge the α, a coordination reaction given below was introduced as shown in formula 4-5.

$$Zn \rightarrow Zn^{2+} + 2e^- \quad (4)$$

$$Zn^{2+} + 4NH_3(aq) \rightarrow [Zn(NH_3)_4]^{2+} \quad (5)$$

As ZnO^{2-} tends to be produced in strong alkaline solution, and at the same time this reaction requires concentrated NH_3(aq) environment, the pH value should be carefully controlled. Consequently, the anolyte was designed as a mixture of 2 M NH_3 and 1 M $(NH_4)_2SO_4$ and 0.1 M

$ZnSO_4$, where the supporting electrolyte $(NH_4)_2SO_4$ was used to adjust the dissociation equilibrium of NH_3, so as to maintain the appropriate pH value. Due to the cathode degradation caused by NH_3 adsorption reaction and the side reaction with hydroxide[20], NiHCF would be dissolved gradually (Supplementary Figure 10). Therefore, the single cation exchange membrane (CEM) or anion exchange membrane (AEM) was not enough to prevent the adsorption of NH_3 and the side reaction. Here, a new design[21] as shown in Figure 1a was used to decouple the electrolyte. In order not to introduce additional evaporation entropy, the measurement was conducted with the strictly sealed cell. Consequently, the measured α of anode originating from reaction entropy change rapidly rises from +0.70 mV K^{-1} to +1.395 mV K^{-1} (+1.248 mV K^{-1} ~ +1.728 mV K^{-1}) as depicted in Figure 1c. The overall α boosted up to -2.270 mV K^{-1} (-2.068 mV K^{-1} ~ -3.004 mV K^{-1}), which is the record-high value in TREC systems (Figure 1d). The fundamental analysis is based on thermodynamics of electrochemistry. Figure 2a depicts the entropy and energy change of the anode, cathode, and the full cell reaction. In short, the increasing temperature lowers the energy gap of the full reaction. The detailed analysis is in Supplementary Note 1.

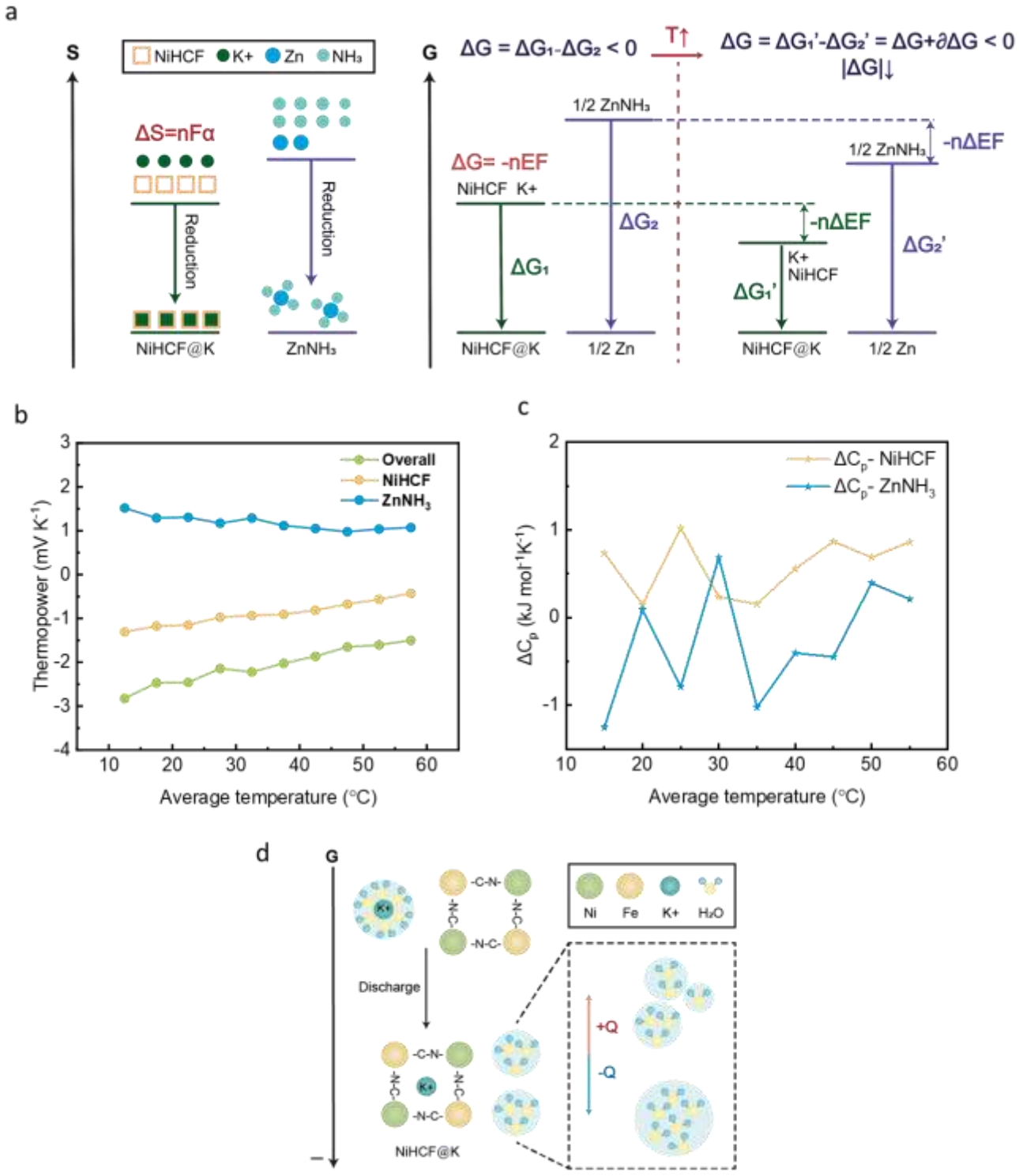

Figure 2. The entropy change and energy change of discharging electrochemical reaction. **a)** Schematic diagram of entropy and energy change of the reaction. **b)** α change of NiHCF and Zn

electrode among the 10℃ to 60℃ temperature range. **c)** Overall heat capacity change $\Delta C_{p_{reaction}}$ of cathode and anode reaction. **d)** Schematic diagram of temperature influence in reaction energy change.

Theoretically, when the activity of solid phase is assumed to be 1, the potential can be calculated from the Nernst equation, and the temperature coefficient is calculated as -0.08617 mV K^{-1} if the activity is approximated to be constant regardless of temperature (Supplementary Note 2). In this work, we found that the α will change with temperature as shown in Figure 2b.

As it is assumed from previous work that the entropy change ΔS is constant, the α is also regarded as a constant according to equation 1. However, it should be noted that the entropy change of the system cannot be simply attributed to entropy change of the electrochemical reaction. While the entropy term in equation 1 is a constant, actually it cannot be decoupled with system energy in non-ideal working fluids.[22] It implies that the entropy change of the reaction ΔS might change since reactants are an indispensable part of the system, yet the entropy of the system usually increases with increasing temperature. Therefore, a modified equation is given as below (Supplementary Note 2):

$$nF\Delta E = \Delta(ST) + R\Delta(T\ln([C^+])) \quad (6)$$

where ΔE is OCV change, R, T, are the gas constant and temperature, and C^+ is the activity of monovalent cation. From the Figure 2c and equation 1, the slope $\frac{\partial \Delta S}{nF\partial T} = \frac{\partial \alpha}{\partial T}$ indicates the reaction entropy change with temperatures. Since the increase of temperature results in smaller water molecular groups,[23] which could be also proved by Raman as shown in Supplementary Figure 3, it illustrates the influence of dehydrated water on the reaction entropy change as depicted in Figure 2d. $\Delta C_{p_{reaction}}$ (is the overall heat capacity change of a reaction) was introduced into this isobaric

system to explore the physical meaning of α change with temperature $\frac{\partial \alpha}{\partial T}$ due to the experimental difficulty in measuring the reaction entropy change (Supplementary Note 4):

$$\Delta C_{p_{reaction}} = \frac{\partial \Delta H}{\partial T} = nFT\left(\frac{\partial \alpha}{\partial T}\right) \quad (7)$$

where ΔH represents reaction enthalpy change. Therefore, the estimated cathode overall reaction heat capacity change is $\Delta C_{p_{reaction}} = 6C_{p_{H_2O}} - C_{p_{[\mathrm{K}(H_2O)_6]^+}}$ as the heat capacities of most metals and simple crystalline solids are similar and stable at room temperature. Since the water heat capacity reaches minimum value of 4.1796 J g^{-1} K^{-1} at 40℃ while the hydration heat capacity $C_{p_{[\mathrm{K}(H_2O)_6]^+}}$ decreases only very slightly with temperature,[24] the theoretical minimum value of overall reaction heat capacity should be obtained at around 40℃ due to the lowest heat capacity of water at ~40℃ (Supplementary Figure 4) which is in line with our results (~35℃) from Figure 2c. The estimated anode reaction heat capacity change is $\Delta C_{p_{reaction}} = 4C_{p_{NH_3H_2O}} + C_{p_{Zn}} - 4C_{p_{H_2O}} - C_{p_{[\mathrm{Zn}(NH_3)_4]^{2+}}} \approx 4C_{p_{NH_3 \cdot H_2O}} - 4C_{p_{H_2O}} + C$, where C is regarded as a constant. The heat capacity change is found to increase with increasing temperature when temperature is higher than 30℃ (Figure 2c) due to the significant increase of $C_{p_{NH_3 \cdot H_2O}}$ with temperature (about 4.2468 J $g^{-1}K^{-1}$ at 10℃, 4.3095 J $g^{-1}K^{-1}$ at 60℃ (10 wt% NH_3)[25]) to $C_{p_{H_2O}}$ (4.1955 J $g^{-1}K^{-1}$ at 10℃, 4.1851 J $g^{-1}K^{-1}$ at 60℃ [26]). However, it is still difficult to quantitatively predict the α change because of unexpectable dissolution and vaporization heat in additional to the heat capacity change (Supplementary Note 4).

To investigate the effects of temperature on the kinetics process and cyclic voltammetry at different temperatures was conducted (Supplementary Figure 5). A series of parameters were analyzed and shown in Figure 3b.

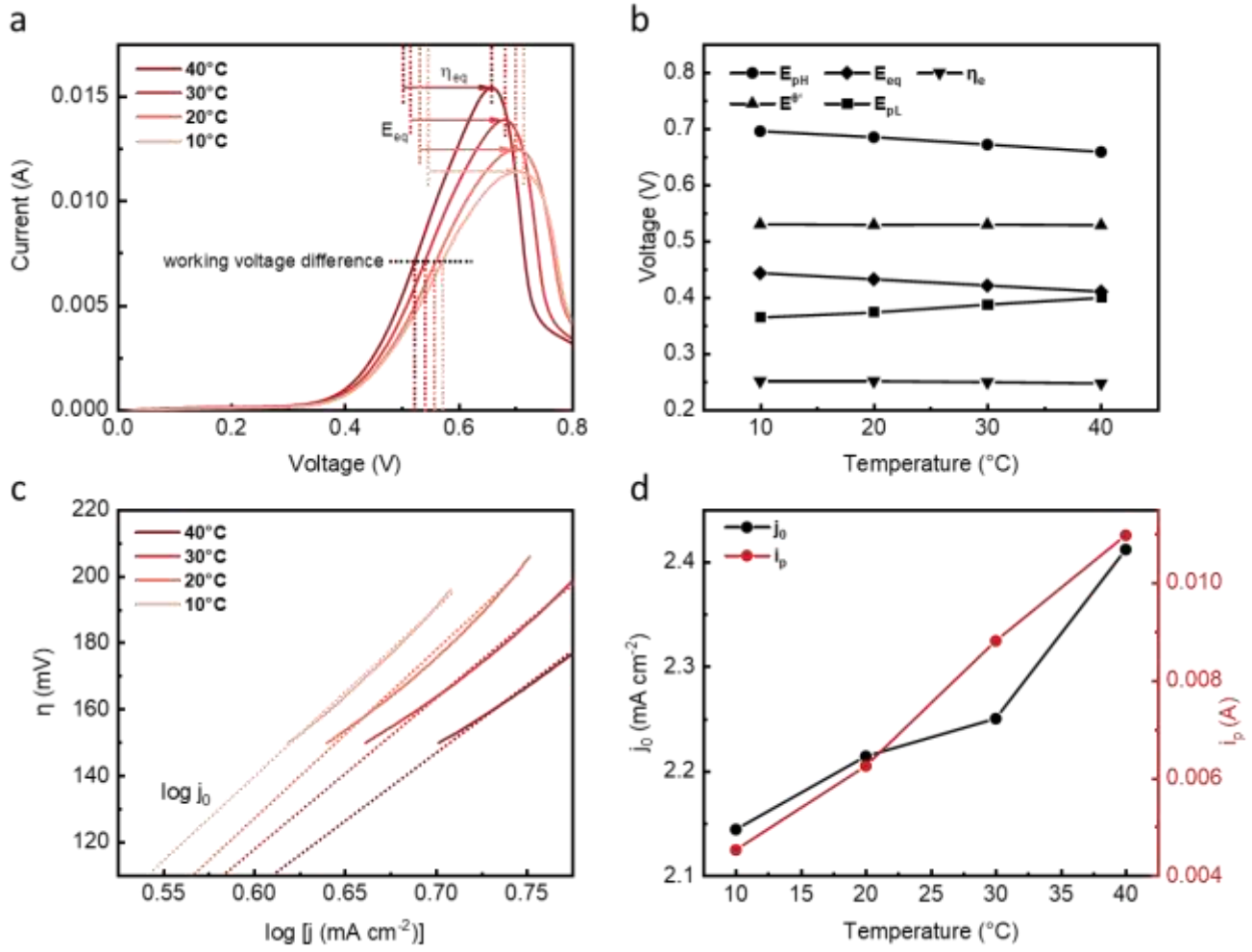

Figure 3. The cyclic voltammetry (CV) curves of NiHCF in 0.5 M K_2SO_4 and kinetics parameters analysis in electrode reaction. **a)** The half CV curve of NiHCF from 10℃ to 40℃ with the sweeping speed of 1 mV s^{-1}. E_{eq} is the equilibrium potential, η_e is the overpotential controlled by charge transfer step. **b)** The various potentials of NiHCF from 10℃ to 40℃. $E^{\theta'}$, E_{pH} and E_{pL} represent formal potential, high and low peak voltage respectively, the sweeping speed is 1 mV s^{-1}. **c)** The linear fitting to extrapolate exchange current density from 10℃ to 40℃. The overpotential can be expressed linearly to lg j where j is current density. The intercept on the x axis represents lg j_0, j_0 is exchange current density. **d)** The obtained exchange current density from Figure 3c and peak current from Figure 3a.

Firstly, the equilibrium potential was measured based on the OCV. The OCV represented the equilibrium state of the electrode when the net current was zero. As the equilibrium potential (E_{eq}) decreased from 0.444 V at 40 ℃ to 0.411 V at 10 ℃ (corresponding to an α of -1.100 mV K^{-1}), the formal potential ($E^{\theta'}$) from CV curve (Supplementary Figure 5) was experimentally measured as the midpoint of two peak voltages (E_{pH} and E_{pL}) and stabilized at approximately 0.530 V vs. Ag/AgCl reference electrode with a small slope of -0.0483 mV K^{-1} from 0.530 V at 10 ℃ to 0.529 V at 40 ℃, as depicted in Figure 3b. The result is consistent with the tendency of calculated temperature coefficient from the coefficient of Nernst equation (-0.08617 mV K^{-1}, Supplementary Note 2).

Secondly, with increasing temperature, the two gradually approaching peaks (E_{pH} and E_{pL} as shown in Supplementary Figure 5) indicated better reversibility, presenting higher exchange current density and reaction rate. Exchange current density was obtained by linear fitting in the overpotential region of 150-200 mV (Figure 3c). The exchange current density increased gradually from 2.145 mA cm^{-2} at 10°C to 2.412 mA cm^{-2} at 40°C, as shown in Figure 3d.

Thirdly, the increasing peak current (Figure 3d) demonstrated higher diffusion rate at higher temperature. For an ion intercalation process, the rate determining step is usually the diffusion movement of ions in the lattice.[27] The peak current i_p can be determined as equation 8 (Randles-Sevcik equation):

$$i_p = 0.4463\, nFAC\left(\frac{nF\nu D}{RT}\right)^{\frac{1}{2}} \quad (8)$$

where A is electrode area, C is electrolyte concentration, ν is scan rate, D is diffusion coefficient and R is the ideal gas constant. The peak current is positively related to $(D/T)^{-1/2}$ at a certain sweeping rate and concentration. As is shown in Figure 3d, the increasing peak current from 0.0119 A to 0.0154 A demonstrated a faster diffusion process and less diffusion overpotential loss at high

temperature. The possible lattice expansion of NiHCF was proved by the peak shift of X-ray Diffraction pattern (Supplementary Figure 6). That attributes to the lattice expansion of NiHCF at a high temperature, leading to faster movement during intercalation.

These results further supported the positive effect of temperature on the kinetic process. A better kinetic performance including better reversibility and lower mass transfer resistance was illustrated by the higher exchange current density and diffusion rate, further confirming that a high temperature facilitates the kinetic process.

For the sake of comprehensive comparison on performance from different aspects, parameters including η (efficiency), η_r (efficiency related to Carnot efficiency), P (power density) will be discussed.

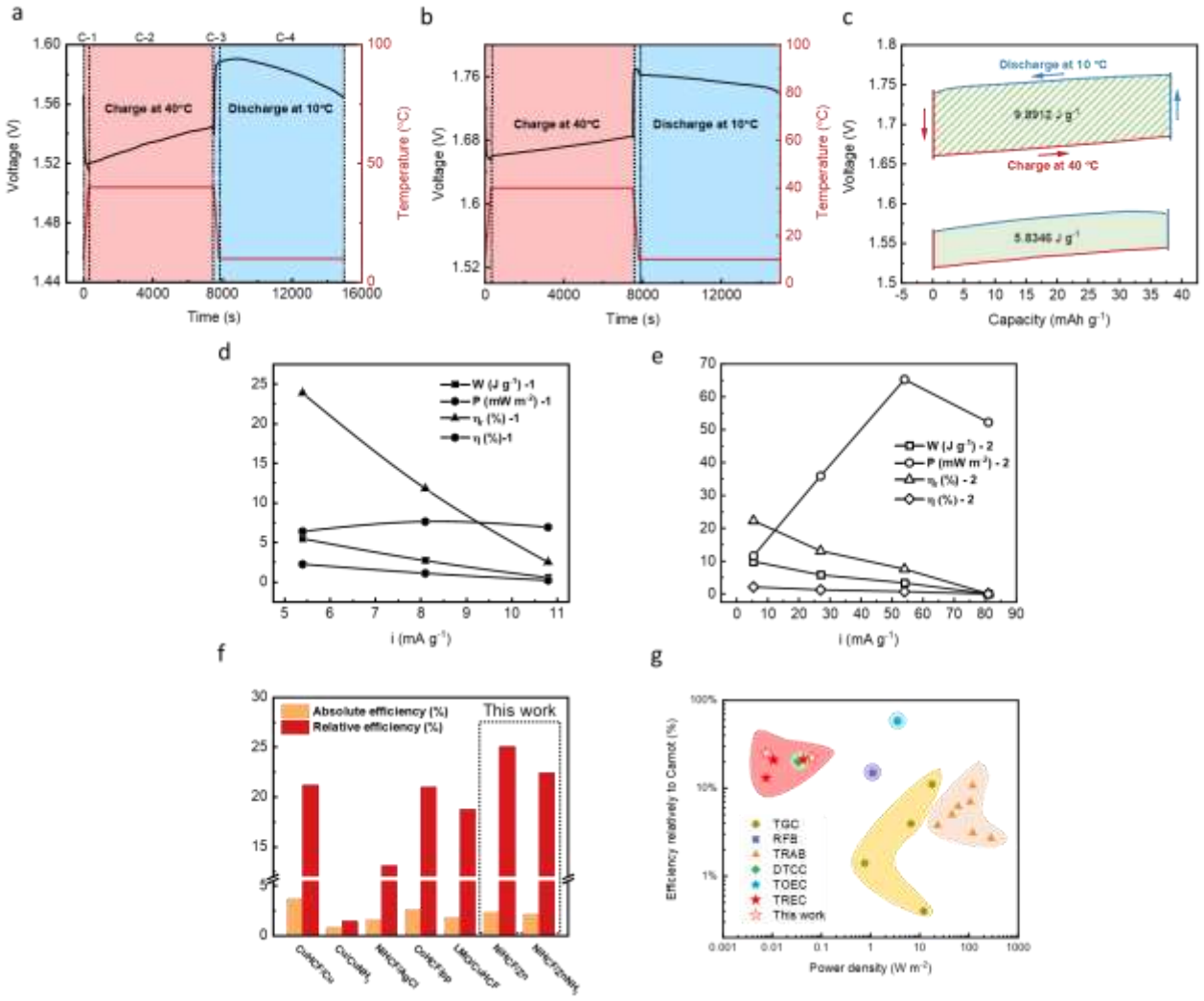

Figure 4. The full cell performance with NiHCF cathode and Zn anode. **a)** The voltage change for the whole cell during a full TREC cycle. The NiHCF-Zn cell was operated between 10°C to 40°C at a current density of 5.4 mA g^{-1}, including C-1 heating up, C-2 charging, C-3 cooling down, and C-4 discharging. **b)** The voltage change for the whole cell during a full TREC cycle. The NiHCF-$ZnNH_3$ cell was operated between 10°C to 40°C at a current density of 5.4 mA g^{-1}. **c)** The full NiHCF/Zn cell capacity plot versus voltage of the whole cycle consistent to Figure 4a and Figure 4b. The corresponding energy density is 5.8346 J g^{-1} (per electrode mass). The full NiHCF/$ZnNH_3$ cell capacity plot versus charging-discharging voltage with 0.1 C current density (5.4 mA g^{-1})

which is as same as the charging-discharging condition as NiHCF-Zn. The corresponding energy density is 9.8912 J g^{-1} (per electrode mass). **d)** The relative efficiency, efficiency, energy density and harvested output power of 0.1 C, 0.15 C, 0.2 C current density with 5.4 mA g^{-1}, 8.1 mA g^{-1}, 10.8 mA g^{-1} within 10°C to 40°C temperature range (η_{HR}=0). 1 represents NiHCF/Zn system. **e)** The relative efficiency, efficiency, energy density and harvested output power at current of 0.1 C (5.4 mA g^{-1}), 0.5 C (27.0 mA g^{-1}), 1 C (54.0 mA g^{-1}), 1.5 C (81 mA g^{-1}) and at temperature gap of 30ºC (10°C to 40°C) (η_{Hr} = 0). 2 represents NiHCF/$ZnNH_3$ system. **f)** The performance comparison including efficiency, relative efficiency and α. The systems include CuHCF/Cu,[10] NiHCF/AgCl,[8] CoHCF/pp[9] and LMO/CuHCF.[19] **g)** The relative efficiency and power density of different systems. Systems include TGC,[5, 28, 29, 30] RFB,[31] TRAB,[12, 13, 14, 15, 16, 17 18] DTCC, [32] TOEC,[3] TREC. [8, 9, 10, 19]

Table 1. The performance comparison. Parameters include α, temperature difference ΔT, energy density W, efficiency η, relative efficiency η_r and recuperation efficiency η_{HR}. The systems include CuHCF/Cu,[10] NiHCF/AgCl,[8] CoHCF/pp[9] and LMO/CuHCF.[19]

System	α_{cell} (mV K^{-1})	ΔT	W J/g	η (%)	η_r (η/η_c , %)	η_{HR}
CuHCF/Cu	-1.2	50.000	5.200	3.7	21.2	0
NiHCF/AgCl	-0.74	40.000	1.000	1.6	13.12	0
CoHCF/pp	-0.89	40.000	2.052	2.65	21	0
LMO/CuHCF	+1.061	30.000	0.970	1.8	21	0
NiHCF/Zn	-1.575	30.000	5.6337	2.40	25.16	0
NiHCF/$ZnNH_3$	-2.270	30.000	9.9502	2.17	22.66	0

The α of the full cell reached -1.575 mV K^{-1}. Assembled TREC full pouch cell was composed of NiHCF cathode, Zn metal anode, and the two electrodes were separated by a normal pp separator which was soaked with 0.5 M K_2SO_4 electrolyte. The electrodes were prepared with an area of 1×2 cm^2 and a material loading of 7 mg cm^{-2} (70% active material of NiHCF) (Supplementary Figure 7). The full cell achieved a high specific capacity of 54 mAh g^{-1} (active material mass) / 37.8 mAh g^{-1} (electrode mass). To enable a complete TREC cycle, the cell was sandwiched between two thermoelectric plates (controlled temperature ± 0.01°C) and two thermocouples were inserted. As is shown in Figure 4a, the cell was heated up to 40°C within 5 minutes, which dramatically decreased the voltage by about 50 mV. The charging process was then implemented at 40ºC under 0.1C current density (equivalent to 5.40 mA g^{-1}) from 80% state of charge to 100% state of charge for 2h. The overpotential was approximately 3.5 mV at the beginning of charging

process and the average charging voltage was 1.5334 V. As shown in Figure 4a-c, after cooling down to 10°C, the discharging process was conducted at the same current density with an average discharging voltage of 1.5814 V and an overpotential of 5 mV. The energy density of 5.8346 J g^{-1} was obtained with the high coulombic efficiency of 99.66%, corresponding to an efficiency of 2.410% and a relative efficiency to Carnot efficiency of 25.155%. The efficiency and relative efficiency were increased to 4.868% and 50.81%, respectively, with a recuperation efficiency of 70%. To examine the current effect, a full cell was tested at 5.40 mA g^{-1}, 8.10 mA g^{-1}, 10.80 mA g^{-1} current density respectively with 30°C temperature difference (Supplementary Figure 8). The larger current density caused higher overpotential.

As shown in Figure 4d, the energy density, efficiency and relative efficiency all decreased almost linearly with current density. At a discharge current of 8.1 mA g^{-1}, the cell achieved the highest power output with good efficiency. The cell can be operated for more than 30 fully charge-discharge cycles (whose time scale equals to 150 cycles of 80% SOC to 100% SOC cycle as shown in Figure 4b) at a current density of 5.4 mA g^{-1}. The fully charged and discharged cell achieved an energy efficiency of 2.30%, which was 24.01% that of the Carnot efficiency. Thanks to excellent coulombic efficiency of NiHCF like Prussian blue analog material,[33] it exhibits good reversibility. However, the side reaction of hydrogen evolution due to the large potential window contributes to additional $Zn(OH)_2$ product, resulting in higher resistance and Ohmic loss, which further decreases the efficiency.

As shown in Supplementary Figure 10, to avoid the side reaction of NH_3 (aq) and NiHCF, the mixed membrane (AEM/CEM) was used to separate the catholyte and anolyte. The same temperature range used for the NiHCF/K_2SO_4/Zn system was adopted to prevent ammonia vaporization. With a higher α of -2.270 mV K^{-1}, a large voltage gap of more than 70 mV was

established with a temperature difference of only 30°C. Thus, a harvested energy density of 9.8912 J g^{-1} is obtained at a discharging voltage of 1.7596 V and a charging voltage of 1.6719 V. As a result, the cell achieved an energy efficiency of 2.171% and a relative efficiency of 22.663% of the Carnot efficiency. With a recuperation efficiency of 70%, a higher energy efficiency of 4.835% was achieved, which corresponded to a relative efficiency of 50.468% of Carnot efficiency (Supplementary Figure 12, Supplementary Note 6). Interestingly, the overpotential in this system is similar to the overpotential in NiHCF/K_2SO_4/Zn system (around 5 mV at 0.1 C) when the same current density is applied. It indicates that the cell resistance not only relies on membrane resistance, but also depends on the concentration of electrolyte. As shown in Figures 4d-e, the maximum power density is almost seven times that of NiHCF/K_2SO_4/Zn system. However, due to the intrinsic diffusion of ammonia, the α and the equilibrium voltage of this system can only be maintained for around 7 cycles. Though different types of strictly sealed cells were tried to prevent the side reaction of NH_3 and NiHCF, the cell capacity degradation happened and the α decreased to around -1.7 mV K^{-1} after a few cycles which similar to the NiHCF/K_2SO_4/Zn system. As depicted in Figure 4f-g, the two systems show great performance in terms of relative efficiency and absolute α.

The energy efficiency highly depends on the temperature gap so that this high efficiency obtained at a 30ºC difference is very satisfactory compared with previous literature (40-50ºC). As the Carnot efficiency represents the maximum efficiency for heat-to-power conversion by a thermodynamic cycle, the relative efficiency to Carnot efficiency was a better indicator to evaluate the performance of the energy system. With the same recuperation efficiency as demonstrated in Figure 4f and Table 1, the reported performance data were summarized and compared. Our two systems perform excellent relative efficiency owning to their high α. Although the power density

is relatively low compared with other systems according to Figure 4g, the design of this work provides a new possibility to further improve the performance.

This study explored the effects of temperature on entropy change and energy change of both systems and electrochemical reactions due to the lack of comprehensive research on the mechanism of heat-to-electricity energy conversion. A theoretical framework was built and equations among a series of thermodynamic parameters were derived in order to illuminate the origins of the α and to identify ways of enhancing the α. We found that the increased temperature changes the reaction heat capacity, which further affects the α. We also investigated the intrinsic energy conversion mechanism including the thermodynamics and kinetics processes. It is found that high temperature has a positive impact on both the thermodynamics and kinetics processes. For thermodynamics process, high temperature lowers the energy gap for heat energy utilization. For kinetics process, high temperature lowers energy gap, accelerates mass transfer process, and lowers overpotential.

To sum up, a fundamental and extended framework of thermo-electrochemical cycle was established in this work. After introducing a new anode reaction, a super high α was obtained by introducing mixed membrane in this mixed pH electrolyte. The mixed membrane design brings more possibilities and inspirations for selecting reactions of TREC to enlarge the α, efficiency and power, which is highly promising for practical industrial application. Note that considering the potential in practical applications, the cost of ion-selective membranes could be reduced by introducing alternative membranes.[2, 13] However, there are still several limitations of cell fabrication which may be solved by substituting the less volatile ligand such as ethylenediamine for the original anolyte. The catholyte also could be replaced by higher concentrated solution like

KCl or KNO_3 in mixed membrane system to further boost up efficiency. Additional work should be done to optimize the structure for durable operation.

ACKNOWLEDGMENTS

M. Ni thanks the funding support from Hong Kong Polytechnic University (P0014036) and a grant (Project Number: PolyU 152064/18E) from Research Grant Council, University Grants Committee, Hong Kong SAR. S. P. Feng thanks the funding support from the General Research Fund of the Research Grants Council under Award Number 17206519.

REFERENCE

(1) Forman, C.; Muritala, I. K.; Pardemann, R.; Meyer, B. Estimating the Global Waste Heat Potential. *Renewable and Sustainable Energy Reviews* **2016**, *57*, 1568–1579. https://doi.org/10.1016/j.rser.2015.12.192.

(2) Rahimi, M.; Straub, A. P.; Zhang, F.; Zhu, X.; Elimelech, M.; Gorski, C. A.; Logan, B. E. Emerging Electrochemical and Membrane-Based Systems to Convert Low-Grade Heat to Electricity. *Energy Environ. Sci.* **2018**, *11* (2), 276–285. https://doi.org/10.1039/C7EE03026F.

(3) Straub, A. P.; Yip, N. Y.; Lin, S.; Lee, J.; Elimelech, M. Harvesting Low-Grade Heat Energy Using Thermo-Osmotic Vapour Transport through Nanoporous Membranes. *Nat Energy* **2016**, *1* (7), 16090. https://doi.org/10.1038/nenergy.2016.90.

(4) Zhang, F.; Liu, J.; Yang, W.; Logan, B. E. A Thermally Regenerative Ammonia-Based Battery for Efficient Harvesting of Low-Grade Thermal Energy as Electrical Power. *Energy Environ. Sci.* **2015**, *8* (1), 343–349. https://doi.org/10.1039/C4EE02824D.

(5) Yu, B.; Duan, J.; Cong, H.; Xie, W.; Liu, R.; Zhuang, X.; Wang, H.; Qi, B.; Xu, M.; Wang, Z. L.; Zhou, J. Thermosensitive Crystallization–Boosted Liquid Thermocells for Low-Grade Heat Harvesting. *Science* **2020**, *370* (6514), 342–346. https://doi.org/10.1126/science.abd6749.

(6) Liu, W.; Jie, Q.; Kim, H. S.; Ren, Z. Current Progress and Future Challenges in Thermoelectric Power Generation: From Materials to Devices. *Acta Materialia* **2015**, *87*, 357–376. https://doi.org/10.1016/j.actamat.2014.12.042.

(7) Gao, C.; Lee, S. W.; Yang, Y. Thermally Regenerative Electrochemical Cycle for Low-Grade Heat Harvesting. *ACS Energy Lett.* **2017**, *2* (10), 2326–2334. https://doi.org/10.1021/acsenergylett.7b00568.

(8) Yang, Y.; Loomis, J.; Ghasemi, H.; Lee, S. W.; Wang, Y. J.; Cui, Y.; Chen, G. Membrane-Free Battery for Harvesting Low-Grade Thermal Energy. *Nano Lett.* **2014**, *14* (11), 6578–6583. https://doi.org/10.1021/nl5032106.

(9) Gao, C.; Yin, Y.; Zheng, L.; Liu, Y.; Sim, S.; He, Y.; Zhu, C.; Liu, Z.; Lee, H.-W.; Yuan, Q.; Lee, S. W. Engineering the Electrochemical Temperature Coefficient for Efficient Low-

Grade Heat Harvesting. *Adv. Funct. Mater.* **2018**, *28* (35), 1803129. https://doi.org/10.1002/adfm.201803129.

(10) Lee, S. W.; Yang, Y.; Lee, H.-W.; Ghasemi, H.; Kraemer, D.; Chen, G.; Cui, Y. An Electrochemical System for Efficiently Harvesting Low-Grade Heat Energy. *Nat Commun* **2014**, *5* (1), 3942. https://doi.org/10.1038/ncomms4942.

(11) Gao, C.; Yin, Y.; Zheng, L.; Liu, Y.; Sim, S.; He, Y.; Zhu, C.; Liu, Z.; Lee, H.-W.; Yuan, Q.; Lee, S. W. Engineering the Electrochemical Temperature Coefficient for Efficient Low-Grade Heat Harvesting. *Adv. Funct. Mater.* **2018**, *28* (35), 1803129. https://doi.org/10.1002/adfm.201803129.

(12) Zhang, F.; Liu, J.; Yang, W.; Logan, B. E. A Thermally Regenerative Ammonia-Based Battery for Efficient Harvesting of Low-Grade Thermal Energy as Electrical Power. *Energy Environ. Sci.* **2015**, *8* (1), 343–349. https://doi.org/10.1039/C4EE02824D.

(13) Rahimi, M.; Zhu, L.; Kowalski, K. L.; Zhu, X.; Gorski, C. A.; Hickner, M. A.; Logan, B. E. Improved Electrical Power Production of Thermally Regenerative Batteries Using a Poly(Phenylene Oxide) Based Anion Exchange Membrane. *Journal of Power Sources* **2017**, *342*, 956–963. https://doi.org/10.1016/j.jpowsour.2017.01.003.

(14) Rahimi, M.; D'Angelo, A.; Gorski, C. A.; Scialdone, O.; Logan, B. E. Electrical Power Production from Low-Grade Waste Heat Using a Thermally Regenerative Ethylenediamine Battery. *Journal of Power Sources* **2017**, *351*, 45–50. https://doi.org/10.1016/j.jpowsour.2017.03.074.

(15) Rahimi, M.; Kim, T.; Gorski, C. A.; Logan, B. E. A Thermally Regenerative Ammonia Battery with Carbon-Silver Electrodes for Converting Low-Grade Waste Heat to Electricity. *Journal of Power Sources* **2018**, *373*, 95–102. https://doi.org/10.1016/j.jpowsour.2017.10.089.

(16) Zhu, X.; Rahimi, M.; Gorski, C. A.; Logan, B. A Thermally-Regenerative Ammonia-Based Flow Battery for Electrical Energy Recovery from Waste Heat. *ChemSusChem* **2016**, *9* (8), 873–879. https://doi.org/10.1002/cssc.201501513.

(17) Wang, W.; Tian, H.; Shu, G.; Huo, D.; Zhang, F.; Zhu, X. A Bimetallic Thermally Regenerative Ammonia-Based Battery for High Power Density and Efficiently Harvesting Low-Grade Thermal Energy. *J. Mater. Chem. A* **2019**, *7* (11), 5991–6000. https://doi.org/10.1039/C8TA10257K.

(18) Wang, W.; Shu, G.; Tian, H.; Huo, D.; Zhu, X. A Bimetallic Thermally-Regenerative Ammonia-Based Flow Battery for Low-Grade Waste Heat Recovery. *Journal of Power Sources* **2019**, *424*, 184–192. https://doi.org/10.1016/j.jpowsour.2019.03.086.

(19) Liu, Y.; Gao, C.; Sim, S.; Kim, M.; Lee, S. W. Lithium Manganese Oxide in an Aqueous Electrochemical System for Low-Grade Thermal Energy Harvesting. *Chem. Mater.* **2019**, *31* (12), 4379–4384. https://doi.org/10.1021/acs.chemmater.9b00310.

(20) Wang, Z.; Yang, H.; Gao, B.; Tong, Y.; Zhang, X.; Su, L. Stability Improvement of Prussian Blue in Nonacidic Solutions via an Electrochemical Post-Treatment Method and the Shape Evolution of Prussian Blue from Nanospheres to Nanocubes. *Analyst* **2014**, *139* (5), 1127. https://doi.org/10.1039/c3an02071a.

(21) Zhong, C.; Liu, B.; Ding, J.; Liu, X.; Zhong, Y.; Li, Y.; Sun, C.; Han, X.; Deng, Y.; Zhao, N.; Hu, W. Decoupling Electrolytes towards Stable and High-Energy Rechargeable Aqueous Zinc–Manganese Dioxide Batteries. *Nat Energy* **2020**, *5* (6), 440–449. https://doi.org/10.1038/s41560-020-0584-y.

(22) Chen, R.; Deng, S.; Xu, W.; Zhao, L. A Graphic Analysis Method of Electrochemical Systems for Low-Grade Heat Harvesting from a Perspective of Thermodynamic Cycles. *Energy* **2020**, *191*, 116547. https://doi.org/10.1016/j.energy.2019.116547.
(23) Starzak, M.; Mathlouthi, M. Cluster Composition of Liquid Water Derived from Laser-Raman Spectra and Molecular Simulation Data. *Food Chemistry* **2003**, *82* (1), 3–22. https://doi.org/10.1016/S0308-8146(02)00584-8.
(24) Marcus, Y. Thermodynamics of Ion Hydration and Its Interpretation in Terms of a Common Model. *Pure and Applied Chemistry* **1987**, *59* (9), 1093–1101. https://doi.org/10.1351/pac198759091093.
(25) Chemical Design Institute of the Ministry of Petrochemical Industry. *Nitrogen Fertilizer Process Design Manual Physical and Chemical Data*; Chemical Industry Press, 1977.
(26) Water - Specific Heat https://www.engineeringtoolbox.com/specific-heat-capacity-water-d_660.html.
(27) Nikitina, V. A.; Vassiliev, S. Y.; Stevenson, K. J. Metal-Ion Coupled Electron Transfer Kinetics in Intercalation-Based Transition Metal Oxides. *Adv. Energy Mater.* **2020**, *10* (22), 1903933. https://doi.org/10.1002/aenm.201903933.
(28) Hu, R.; Cola, B. A.; Haram, N.; Barisci, J. N.; Lee, S.; Stoughton, S.; Wallace, G.; Too, C.; Thomas, M.; Gestos, A.; Cruz, M. E. dela; Ferraris, J. P.; Zakhidov, A. A.; Baughman, R. H. Harvesting Waste Thermal Energy Using a Carbon-Nanotube-Based Thermo-Electrochemical Cell. *Nano Lett.* **2010**, *10* (3), 838–846. https://doi.org/10.1021/nl903267n.
(29) Zhang, L.; Kim, T.; Li, N.; Kang, T. J.; Chen, J.; Pringle, J. M.; Zhang, M.; Kazim, A. H.; Fang, S.; Haines, C.; Al-Masri, D.; Cola, B. A.; Razal, J. M.; Di, J.; Beirne, S.; MacFarlane, D. R.; Gonzalez-Martin, A.; Mathew, S.; Kim, Y. H.; Wallace, G.; Baughman, R. H. High Power Density Electrochemical Thermocells for Inexpensively Harvesting Low-Grade Thermal Energy. *Adv. Mater.* **2017**, *29* (12), 1605652. https://doi.org/10.1002/adma.201605652.
(30) Im, H.; Kim, T.; Song, H.; Choi, J.; Park, J. S.; Ovalle-Robles, R.; Yang, H. D.; Kihm, K. D.; Baughman, R. H.; Lee, H. H.; Kang, T. J.; Kim, Y. H. High-Efficiency Electrochemical Thermal Energy Harvester Using Carbon Nanotube Aerogel Sheet Electrodes. *Nat Commun* **2016**, *7* (1), 10600. https://doi.org/10.1038/ncomms10600.
(31) Poletayev, A. D.; McKay, I. S.; Chueh, W. C.; Majumdar, A. Continuous Electrochemical Heat Engines. *Energy Environ. Sci.* **2018**, *11* (10), 2964–2971. https://doi.org/10.1039/C8EE01137K.
(32) Wang, X.; Huang, Y.-T.; Liu, C.; Mu, K.; Li, K. H.; Wang, S.; Yang, Y.; Wang, L.; Su, C.-H.; Feng, S.-P. Direct Thermal Charging Cell for Converting Low-Grade Heat to Electricity. *Nat Commun* **2019**, *10* (1), 4151. https://doi.org/10.1038/s41467-019-12144-2.
(33) Ao, H.; Zhao, Y.; Zhou, J.; Cai, W.; Zhang, X.; Zhu, Y.; Qian, Y. Rechargeable Aqueous Hybrid Ion Batteries: Developments and Prospects. *J. Mater. Chem. A* **2019**, *7* (32), 18708–18734. https://doi.org/10.1039/C9TA06433H.